applied optics

Development of an optical microscopy system for automated bubble cloud analysis

DANIEL J. WESLEY, DANIEL T. W. TOOLAN, STUART A. BRITTLE, JONATHAN R. HOWSE,* AND WILLIAM B. ZIMMERMAN

University of Sheffield, Department of Chemical and Biological Engineering, Mappin Street, Sheffield S1 3 JD, UK
**Corresponding author: j.r.howse@sheffield.ac.uk*

Received 11 March 2016; revised 21 June 2016; accepted 22 June 2016; posted 8 July 2016 (Doc. ID 260966); published 1 August 2016

Recently, the number of uses of bubbles has begun to increase dramatically, with medicine, biofuel production, and wastewater treatment just some of the industries taking advantage of bubble properties, such as high mass transfer. As a result, more and more focus is being placed on the understanding and control of bubble formation processes and there are currently numerous techniques utilized to facilitate this understanding. Acoustic bubble sizing (ABS) and laser scattering techniques are able to provide information regarding bubble size and size distribution with minimal data processing, a major advantage over current optical-based direct imaging approaches. This paper demonstrates how direct bubble-imaging methods can be improved upon to yield high levels of automation and thus data comparable to ABS and laser scattering. We also discuss the added benefits of the direct imaging approaches and how it is possible to obtain considerable additional information above and beyond that which ABS and laser scattering can supply. This work could easily be exploited by both industrial-scale operations and small-scale laboratory studies, as this straightforward and cost-effective approach is highly transferrable and intuitive to use.

OCIS codes: (100.0100) Image processing; (100.2960) Image analysis; (150.0150) Machine vision; (150.2950) Illumination; (180.0180) Microscopy; (150.2945) Illumination design.
http://dx.doi.org/10.1364/AO.55.006102

1. INTRODUCTION

Over recent years the use of microbubbles in commercial applications has attracted major interest in areas such as medical imaging, drug delivery, algal growth, biofuel production, and emulsion separation. This has led to a requirement for a deeper understanding of the bubble formation process. Microbubbles, defined by the size range of 1–999 mm have been extensively studied, with industries such as pharmaceuticals, food technology, biotechnology, and medicine taking advantage of the bubble properties.

Microbubbles are more desirable than fine (mm sized) bubbles due to their increased ability to facilitate high levels of mass transfer. Mass transfer, the movement of mass from one location to another, is directly related to the interfacial area between two locations/phases, etc. This is characterized by Eq. (1) below.

$$J = K_l S(c_g - c_l), \tag{1}$$

where J is the interphase mass transfer flux (moles per second), K_l is the mass transfer coefficient (m/s), S is the interfacial area (m^2), and c_g and c_l are the molar concentrations of gas and liquid, respectively [1].

As can be seen from (1) an increase in the interfacial area leads to an increase in the mass transfer flux between the bubble and its surroundings. The spherical shape of the stable bubble leads to an inverse relationship between the surface-area-to-volume ratio and the bubble radius. This means as an equal volume of gas is split into smaller and smaller bubbles, the available interfacial area to facilitate mass transfer increases dramatically.

Despite the broad range of uses for microbubbles, algal growth for biofuel production is currently at the forefront of global research. The movement away from fossil fuels to cleaner, more sustainable forms of energy has been driven by the unsustainability of current fossil fuel usage, and also the global environmental impact these fuels have. Currently, it is estimated between 65%–80% of the global energy demand is met by conventional fossil fuels [2–4]. Despite this knowledge, many current renewable energy sources such as solar power, wind energy, hydroelectricity, and geothermal all focus on production of electricity. As a result, more and more attention is being placed on biofuels, such as biodiesel, to satisfy the energy requirements of the planet. Unfortunately, current processes are very inefficient at converting solar energy to biofuel, with numerous studies discussing the inherent problems of biofuel production, and steps being undertaken to increase proliferation with the addition of microbubbles [1,3,5–12].

1559-128X/16/226102-06 Journal © 2016 Optical Society of America

Algal separation and harvesting is one of the key challenges to the commercial viability of biofuel production. Once again microbubbles have been utilized to increase the separation efficiency. Gudin and Thepenier [13] estimates that the harvesting step could account for 20%–30% of the total energy usage in biofuel production, although Molina stipulates this figure could be much higher, and as large as 60% [14]. Historically separation has been carried out by flocculation and bioflocculation followed by sedimentation. A development using the Jameson cell in an induced air flotation (IAF) step, this process could reach high yields of up to 98% algal separation. Other techniques, such as dissolved air flotation (DAF) and dispersed air flotation have also been tested as possible routes for algal separation. However, all of these techniques have drawbacks when compared to microflotation. Microbubble generation by a robust technique, such as the fluidic oscillator systems presented by Zimmerman and Tesař [15–18], have proven to be a breakthrough in energy-efficient separation. Tailoring conditions such as flow rate, pressure, and frequency, the bubble size can be tuned to meet the specific needs of each individual system. In addition, the no-moving-part nature and robustness of the oscillator leads to energy usage 2 or 3 times lower than that used in DAF and dispersed air flotation, for example [19]. In the work by Hanotu *et al.* [19] microflotation was presented as a viable alternative for algal separation, finding that separation efficiencies of more than 96% could be achieved with the fluidic oscillator, in addition to the significant energy savings.

Due to the growing commercial applications, it is important to understand and characterize bubble growth and formation in order to control it. There are numerous characterization techniques available, with several briefly reviewed here.

2. ACOUSTIC BUBBLE MEASUREMENT

Bubbles may be measured by the application of acoustic waves to the medium under investigation and monitoring the attenuation, velocity, and amplitude changes exhibited by the acoustic wave as it passes through the bubbling media. Short monochromatic bursts of sound are emitted from a hydrophone, situated within the sample liquid, and pass through the media to a second detector hydrophone. Bubbles influence both the velocity and amplitude of the wave traveling between the emitter and detector, and size distribution calculations are carried out using the dispersion relation [20]. Each bubble has a characteristic resonance frequency, at which the attenuation of the wave is strongest. A frequency sweep is carried out, and bubbles interact with each frequency to a greater or lesser extent based upon size. It is these interactions which are detected and amplified to yield bubble size distributions. Bubble sizes in the range of 34–1200 μm are often encompassed in acoustic study, although the range can be altered through the application of different hydrophones and frequency pulses.

A. Light Scattering

This technique is based on light blocking or dark-field specular reflectometry. A laser beam is sent into the sample where it is reflected and refracted by the particulates, whether they are bubbles or solids. The reflected and refracted light is captured by a photodetector and the signal is intensified by a photomultiplier. The detected signals are sorted by height by the autocorrelation function, and most often the Stokes–Einstein equation is applied to relate the particle motion (often Brownian motion) to the particle size. The size of the particles must be larger than that of the incoming polarized light, allowing the technique to probe down to the nanometer size region.

B. Direct Bubble Imaging

Direct imaging experimental techniques for bubble analysis can vary greatly depending upon the camera, lighting conditions, and lens used. However, in general the bubble size range that can be investigated is similar to that of acoustic-based methods, with the sampling area somewhere between the acoustic and light scattering techniques. The factors effecting bubble imaging and measurement are discussed later.

3. SCOPE OF THIS PAPER

As can be seen from Table 1, direct imaging approaches have the potential to provide a greater range of information regarding microbubble properties compared to both acoustic and light scattering techniques. The extended data set obtainable from imaging-based methods is highly desirable for increasing the understanding of bubbling through both viscous and inviscid media. In addition, direct imaging approaches hold potential applications in algal floc analysis during microflotation, which would allow simultaneous analysis of both the bubble cloud, the floc, and interactions between the two. This would then enable improvements in algal separation to be made and, as such, lead to large increases in the commercial viability of biofuels. Despite the potential of direct imaging approaches, the slow manual data analysis is a major drawback limiting current applications.

While there are a number acoustic- and laser-based systems available commercially, direct imaging of microbubbles, via optical-based techniques, often need to be developed *in house*. This work aims to cover the key aspects of developing an optical imaging set-up, with fully automated analysis protocols that

Table 1. Comparison of the Three Major Bubble Sizing Techniques

Analysis Technique	Size Range (μm)	Analysis Speed	Data Output	Other Pros and Cons
Acoustic	34–1200	Fast and highly automated	Size, Size distribution	Can be used in non-transparent media. High cost. Limited data output.
Light scattering	<100	Fast and automated	Size, Size distribution	Small range. Limited output.
Photographic (optical)	>50	Slow and manual	Size, Size distribution, Rise velocity, Shape analysis, Formation process	Increased information, easily modifiable, relatively low cost, viscous liquids may be used

enable a wealth of information regarding microbubble behavior to be obtained.

4. EXPERIMENTAL SET-UP

This paper aims to provide a framework for selecting appropriate components to develop a set-up to enable automated microbubble image analysis.

The microbubble imaging approach used here for demonstration of the acquisition of high-quality microbubble images consists of a Mikrotron MC1363 Eosens camera with a 22.9 mm CMOS chip (14 μm square pixel size), Nikon AF Nikkor 70-210 mm, 1:4-5.6, bubble specimen tank, and an array of 7 Bridgelux BXRA-56C9000-J-00 high-brightness LED's (cool white, 5600 K, 9000 lm) and is shown schematically in Fig. 1(a). The system was focused on the plane running through the center of the orifice plate. Microbubble images were analyzed using custom-made LabVIEW software, details of which are discussed in detail in the preceding paper and are available to download according to Code 1, Ref. [31], Code 2, Ref. [32], and Code 3, Ref. [33] below.

A. Image Capture—Illumination Conditions

For microbubble applications, optimal contrast between the media and bubble is most easily obtained when brightfield lighting conditions are utilized. In such cases, a set-up may comprise camera + objective + sample + illumination source. High-quality images of bubbles are defined as those where the bubble/media interface is sharp and there is high contrast between the bubble and the media (e.g., large difference in intensity between two phases). A high-contrast image of a microbubble cloud is shown in Fig. 1(b). Such backlighting approaches have been found to yield images with high contrast "doughnut" shaped particles, facilitating accurate post-process analysis of the imaged bubbles. It is important to utilize a light source with sufficient intensity to yield such high contrast between the subject and the background. In addition, high-intensity light sources enable the camera to run at lower exposure times and with smaller aperture sizes. Reduction in exposure (the time which the image sensor is exposed), limits the movement of the rising bubble during the acquisition time and thus reduces any blurring/streaking of bubble features. The use of a smaller aperture increases the depth of field, which in turn allows an increased level of focus throughout the image, leading to a more accurate representation of bubble features.

The type of light source employed is also an important consideration during image capture. For acquisition carried out at moderate to high frame rates, conventional halogen lighting is not suitable due to its inherent flickering at 50 Hz arising from the alternating current of the power supply. As such, if the image acquisition frame rate is not matched to the frequency of the illumination source, there are periodic intensity shifts (from bright to dark). Such periodic alterations in image intensity are likely to hamper any automated image analysis protocols as thresholding conditions, which are used to distinguish image features, must be continually adapted. Thresholding can utilize many algorithms to determine whether a pixel is part of a particle or part of the background. High-contrast bubble images enable greater distinction between the bubble and media during the thresholding step, thus allows greater accuracy in particle size determination post-thresholding.

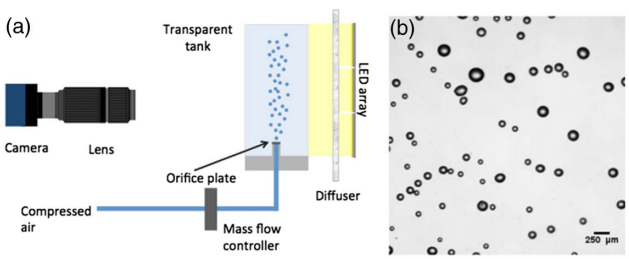

Fig. 1. (a) Schematic of microbubble imaging set-up and (b) high-contrast image of a bubble cloud.

LED illumination sources are able to provide constant irradiation without the periodic intensity fluctuations of halogen sources. LEDs may be arranged into arrays in order to produce large areas of uniform illumination, which can be adjusted in accordance with the supplied power. When utilizing such LED arrays, depending upon the distance between the sample and the LED array, a diffuser may be required to increase illumination uniformity. Further, LEDs are available with a wide range of emission wavelengths and spectral widths that may be selected to match the spectral response of an image sensor.

B. Image Capture—Camera Considerations

The quality of the images acquired is a determined by all the components making up the optical imaging set-up, including illumination conditions, lens magnification, numerical aperture, image sensor size (pixel size × number of pixels), and the consequent signal-to-noise ratio (SNR). The SNR represents the ratio of the measured light signal to sources of noise and a large signal-to-noise ratio is important for the acquisition of high-quality bubble images. The SNR may be written as in Eq. (2) below, which is structured as a ratio of total signal generated during exposure divided by various noise components:

$$\mathrm{SNR} = \frac{PQ_e t}{[PQ_e t + \mathrm{Dt} + N_r^2]^{1/2}}, \tag{2}$$

where P is the incident photon flux (photons/pixel/second), Q_e represents the CCD quantum efficiency, t is the integration time (seconds), D is the dark current value (electrons/pixel/second), and N_r represents read noise (electrons rms/pixel).

The three common sources of noise are photon noise (or short noise), dark current, and read noise. The short noise is a function of the Poisson statistical distribution of photons incident on the image sensor and is equivalent to the square root of the signal. The dark current is a measure of the thermally induced signal and is often reduced by using cooled image sensors. The read noise arises from the system components that turn the incident photons into a measurable voltage.

An important aspect to consider is how the image data is read off the camera sensor. The two most common modes are rolling and global shutter. In rolling shutter, lines of the image sensor array are sequentially read at different times as a readout "wave" sweeps across the sensor. As such, each row of the image sensor will start and end its exposure at different times, which can lead to spatial distortion of the acquired images, especially when studying fast-moving objects, such as

swimmers. In global shutter mode, all of the pixels in the image sensor are exposed simultaneously and so can be thought of as a snapshot or "freeze frame" mode. The differences between rolling and global shutter modes are best demonstrated considering the acquisition of images of fast-moving objects. For fast-moving objects (i.e., bubbles rising through a medium) images taken using rolling shutter may exhibit large spatial distortions, as the bubbles may move faster than the sequential sensor readout, while the global shutter images will be free from any spatial distortion. As such, for studying microbubbles, a global shutter is preferred as it enables the entire field of view to be temporally correlated.

The image series acquisition rate should also be considered when imaging dynamic bubble behavior, such as microbubble formation or bubble interactions. The maximum frame rate is usually limited by the rate of data transfer between the camera and computer. As such, the frame rate is a factor of the field of view, with smaller fields of view enabling faster frame rates. This has an impact on the type of camera you choose to use. A CCD camera generally has a higher sensitivity compared to a CMOS-based camera. However, the field of view is more flexible on CMOS-based cameras due to the image sensor architecture. In addition, there is usually a trade-off between the total observed field of view and the duration of the image series acquisition possible. For example, fast-moving microbubbles will quickly move out of a small field of view, preventing the measurement of rise velocities.

A further consideration is the choice between a monochromatic and color camera system. It is often the case that monochromatic cameras have a higher sensitivity than color cameras, making monochrome a more logical choice for low lighting conditions, or conditions where high levels of illumination and contrast are required. Furthermore, the image bit depth is an important consideration. Higher bit depths yield images with more subtle tonal difference and the user must determine if this subtlety is necessary at the expense of write speed and file size. The region of interest multiplied by the bit depth gives the number of bits per frame captured during acquisition. If static images are captured, this corresponds to the uncompressed file size. If a video is captured during acquisition, the number of frames is multiplied by this number to yield the file size. Therefore, the region of interest, bit depth, and frame rate must all be considered during acquisition to ensure the data may be written without frame "dropping" and data loss.

C. Post-processing Bubble Image Analysis

The direct bubble imaging set-up demonstrated here allows the acquisition of a large series of high-quality images that must be analyzed in order to obtain quantitative data regarding bubble properties. To facilitate automated image analysis, a custom-made bubble analysis program was developed using Laboratory Virtual Instrument Engineering Workbench (LabVIEW) and is the focus this section.

1. Removal of Edge Effects

Any objects in contact with the edge of the frame under investigation are eliminated from the analysis process. Using a connectivity algorithm, LabVIEW can remove objects based on the surrounding pixels. For example, a pixel labeled P_0 has 8 surrounding pixels, P_1 to P_8, as shown in Eq. (3). Mathematically the pixels P_1, P_3, P_5, and P_7 are closer to P_0 than the other pixels. If we define the distance between P_0 and P_1 to be D, then the distance from P_0 and P_2 is $\sqrt{2}*D$. This gives the user the option to utilize connectivity-4, where the pixel under examination must be a distance D from the original pixel, or connectivity-8, where the pixel under examination must be either D or $\sqrt{2}*D$ from the original pixel.

$$\begin{bmatrix} P_8 & P_1 & P_2 \\ P_7 & P_0 & P_3 \\ P_6 & P_5 & P_4 \end{bmatrix}. \tag{3}$$

This algorithm acts to remove edge defects from the image before analysis. This is of vital importance to ensure accurate analysis can be carried out.

2. Treatment of Overlapping Bubbles

When a bubble cloud becomes highly concentrated it becomes increasingly unlikely that bubbles do not overlap within the frame. Overlapping bubbles could comprise of just two individuals or may extend to large numbers depending on the conditions used. Due to the highly autonomous nature of the analysis technique presented herein, the authors feel the removal of these overlapping particles is vindicated by the incredibly large dataset still in existence after removal. However, it is possible to separate the particles into the constituent parts using complex algorithms. The first method utilizes the Danielsson function to recreate concentric circles within each particle and allows the particle shape to be determined. The circulatory factor allows the user to decide how much deviation from sphericity to allow the analysis algorithm, utilizing a ratio of the maximum radii and minimum radii. Particles exceeding the circularity factor are eliminated from the analysis, before the reconstruction takes place, with the result shown in Fig. 2.

5. PARTICLE ANALYSIS

Particle analysis parameters may be set by the user and can yield numerous data outputs. These include the maximum radius and the minimum radius, the area of the particle, the moment of inertia, and the position of the particle center as a pixel coordinate (X, Y). This enables the user to access considerably more data than both the ABS and laser scattering techniques discussed previously. Some useful information obtained is summarized below.

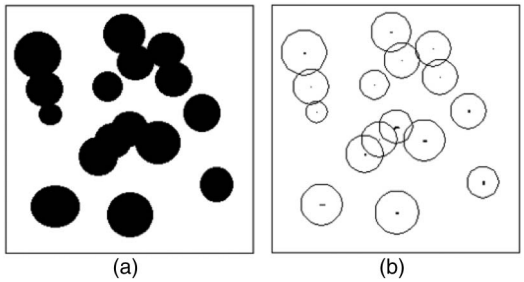

Fig. 2. Danielsson reconstruction of particle forms from overlapping circular features. (a) The overlapping particles are extrapolated into separate ones by the algorithm (b).

A. Particle Size Measurement

Particle size measurement was carried out utilizing the Danielsson algorithm coupled with an in-frame calibration, the results of which are shown in Fig. 3 for a "pointfour" diffuser disk (25 mm diameter, 3 mm thick) under a steady 2.5 mL/min flow of air into water. It can be seen that the distribution and mean size of 0.166 ± 0.059 mm can be achieved from the bubble cloud analysis. This sample set encompassed ca 400,000 bubbles in the analysis, which clearly removes the tedious nature of the analysis process. The sample size also brings the direct imaging technique into line with ABS and laser scattering studies and removes the advantage of these techniques over the optical-based methods.

In addition to the straightforward approach outlined above, it is also possible to build in other statistical tests and methodologies to generate automated measurement/statistical analysis systems. For example, determination of the mean bubble size may be performed using the common D [1,0] method as shown in Eq. (4), where D is the individual bubble diameter and n is the total number of bubbles. The D [1,0] method of calculating average bubble diameter is chosen for simplicity, and to quickly represent any changes in bubble diameter that may occur as a result of system parameter alterations [21]:

$$D[1,0] = \frac{\sum_1^n D}{n}. \tag{4}$$

However, the more complex Sauter mean diameter D [3,2] is also a well-known method of estimating average particle size and may be calculated using Eq. (5) [21]:

$$D[3,2] = \frac{\sum_1^n 6v/A}{n}, \tag{5}$$

where V and A are the particle volume and surface area, respectively.

B. Bubble Rise Velocity

In addition to the bubble size distribution and determination of the D [1,0] diameter, bubble rise velocity may also be determined. Utilizing the same images as the previous analysis, the (X, Y) coordinates of the bubble centers may be extracted from each frame. Using tracking techniques discussed by Dunderdale *et al.* [22] it is possible to convert these coordinates into trajectories for the rising bubble. Utilizing the simple Pythagorean theorem, the distance traveled vertically between frames by each bubble can be readily determined, and as such the rise velocity can be calculated. Coupling this information with the sizing component of the software, the dependence of rise velocity on size can be established, as shown in Fig. 4. A bubble with a diameter of 0.30 mm has a rise velocity of 13.9 mm/s, a 0.70 mm bubble rises at 25.7 mm/s, a 1.33 mm bubble rises at 41.6 mm/s, a 1.95 mm bubble rises at 65.1 mm/s, and a 2.25 mm bubble rises at 98.2 mm/s.

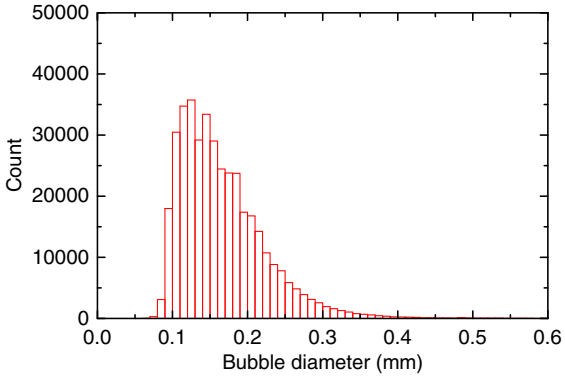

Fig. 3. Bubble size distribution of a "pointfour" diffuser disk (25 mm diameter, 3 mm thick) under a steady 2.5 mL/min flow of air into water.

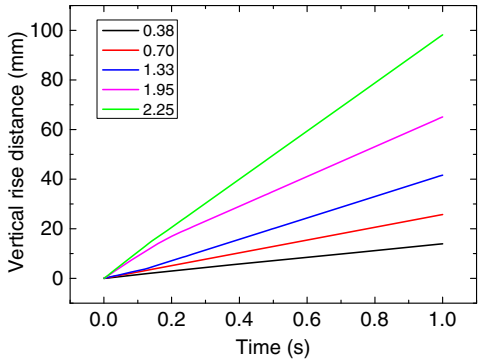

Fig. 4. Dependence of rise velocity on bubbles size (mm). Vertical travel was calculated from the (X, Y) coordinates of the rising bubble centers. Bubble size was taken as the mean of the largest and smallest radii of each bubble. A bubble with a diameter of 0.38 mm (black) has a rise velocity of 13.9 mm/s; a 0.70 mm bubble (red) rises at 25.7 mm/s; a 1.33 mm bubble (blue) rises at 41.6 mm/s; a 1.95 mm bubble (pink) rises at 65.1 mm/s; and a 2.25 mm bubble (green) rises at 98.2 mm/s.

6. FURTHER ADAPTATIONS AND USES

In addition to the bubble size and the bubble rise velocity determination outlined, optical systems also hold significant advantages over other systems due to their ability to be readily modified. The system may be altered to output many parameters and the use of the developed LabVIEW-based bubble analysis processing tool gives the user the ability to tailor the analysis to specific requirements. In addition, the analysis may be performed post–image capture or in-line, facilitating real-time data analysis. This may be of use during many investigations, such as acoustic streaming [23–26] and oscillatory bubble formation [10,15,16,27–29], as well as to explore viscosity effects and flow rate effects. Similarly, the algal growth for biofuels and the oil emulsion separation industries can benefit from the system by not only obtaining bubble size and size distribution data, but also live images of the interaction between bubbles and flocculated particulates. This data has been shown to be of great importance in previous works [1,10,12,19,28,30] to understand the separation processes inherent within these industries. The optical-based approaches provide a convenient, cost-effective way to attain both data sets within a single system.

7. CONCLUSIONS

This study has shown how an optical characterization system may be established and utilized to bring the previously tedious

optical analysis of bubble clouds to a level of automation previously seen in other high-cost systems such as ABS and laser scattering. The optical system must be optimized and tailored to suit the end goals of the user in order to maximize the usefulness of the process. Once optimized, it has been shown that an optical-based system can be used to surpass the other systems and be applied to a wider range of applications. Combined with the LabVIEW-based bubble analysis software, the implementation of in-line statistical analysis may be achieved, as can post-capture analysis. In addition, the optical system allows dynamic data analysis and as a result, effects such as viscosity or flow rate can be adjusted and the effect on bubble formation monitored in real time. Finally, the optical system provides the user with not only numerical data such as average bubble size and size distribution, but it also provides more qualitative data. The interaction of microbubbles with algal and oil flocs in biofuel production and emulsion separation, respectively, has been shown to be of major importance in both industries. Optical-based imaging methods give the user the ability to monitor this interaction while the quantitative data is being accrued, a significant benefit that cannot be provided by ABS or laser scattering experiments.

In conclusion, we have demonstrated how optical analysis systems can be established and utilized as a straightforward, low-cost alternative to the commonly used ABS and laser scattering techniques. We have also demonstrated how, with minor tweaks, the system can be altered to yield results not possible with other techniques. This paves the way for further research to be conducted into many aspects of the bubble formation process, optimizing aspects of globally important industries in the process.

Funding. Engineering and Physical Sciences Research Council (EPSRC) (R/128-872-11-1, EP/I019790/1 and EP/K001329/1).

REFERENCES

1. W. B. Zimmerman, B. N. Hewakandamby, V. Tesař, H. C. H. Bandulasena, and O. A. Omotowa, "On the design and simulation of an airlift loop bioreactor with microbubble generation by fluidic oscillation," Food Bioprod. Process. **87**, 215–227 (2009).
2. J. C. Quinn and R. Davis, "The potentials and challenges of algae based biofuels: a review of the techno-economic, life cycle, and resource assessment modeling," Bioresour. Technol. **184**, 444–452 (2015).
3. P. M. Schenk, S. R. Thomas-Hall, E. Stephens, U. C. Marx, J. H. Mussgnug, C. Posten, O. Kruse, and B. Hankamer, "Second generation biofuels: high-efficiency microalgae for biodiesel production," BioEnergy Res. **1**, 20–43 (2008).
4. G. Mao, X. Liu, H. Du, J. Zuo, and L. Wang, "Way forward for alternative energy research: a bibliometric analysis during 1994–2013," Renewable Sustainable Energy Rev. **48**, 276–286 (2015).
5. D. Das and T. N. Veziroğlu, "Hydrogen production by biological processes: a survey of literature," Int. J. Hydrogen Energy **26**, 13–28 (2001).
6. H. Gaffron and J. Rubin, "Fermentative and photochemical production of hydrogen in algae," J. Gen. Physiol. **26**, 219–240 (1942).
7. B. Hankamer, F. Lehr, J. Rupprecht, J. H. Mussgnug, C. Posten, and O. Kruse, "Photosynthetic biomass and H2 production by green algae: from bioengineering to bioreactor scale-up," Physiol. Plant. **131**, 10–21 (2007).
8. A. Melis, L. Zhang, M. Forestier, M. L. Ghirardi, and M. Seibert, "Sustained photobiological hydrogen gas production upon reversible inactivation of oxygen evolution in the green Alga Chlamydomonas reinhardtii," Plant Physiol. **122**, 127–136 (2000).
9. S. T. Jones, "Gas-liquid mass transfer in an external airlift loop reactor for syngas fermentation: ProQuest," in *Retrospective Theses and Dissertations* (2007), paper 15547, http://lib.dr.iastate.edu/rtd/15547.
10. W. B. Zimmerman, M. Zandi, H. C. Hemaka Bandulasena, V. Tesař, D. James Gilmour, and K. Ying, "Design of an airlift loop bioreactor and pilot scales studies with fluidic oscillator induced microbubbles for growth of a microalgae Dunaliella salina," Appl. Energy **88**, 3357–3369 (2011).
11. J. Hanotu, "Algal growth enhancement mediated by CO_2 enriched microbubbles," M.Sc. dissertation (Environmental and Energy Engineering, University of Sheffield, 2009).
12. K. Ying, D. J. Gilmour, Y. Shi, and W. B. Zimmerman, "Growth enhancement of Dunaliella salina by microbubble induced airlift loop bioreactor (ALB)—the relation between mass transfer and growth rate," J. Biomater. Nanobiotechnol. **4**, 1–9 (2013).
13. C. Gudin and C. Thepenier, "Bioconversion of solar energy into organic chemicals by microalgae," Adv. Biotechnol. Processes **6**, 73–110 (1986).
14. E. M. Grima, E.-H. Belarbi, F. A. Fernández, A. R. Medina, and Y. Chisti, "Recovery of microalgal biomass and metabolites: process options and economics," Biotechnol. Adv. **20**, 491–515 (2003).
15. V. Tesař, C.-H. Hung, and W. B. Zimmerman, "No-moving-part hybrid-synthetic jet actuator," Sens. Actuators A **125**, 159–169 (2006).
16. W. B. Zimmerman, V. Tesař, and H. C. H. Bandulasena, "Towards energy efficient nanobubble generation with fluidic oscillation," Curr. Opin. Colloid Interface Sci. **16**, 350–356 (2011).
17. V. Tesař, "Configurations of fluidic actuators for generating hybrid-synthetic jets," Sens. Actuators A **138**, 394–403 (2007).
18. V. Tesař, "Microbubble generation by fluidics. Part I: development of the oscillator," in *Colloquium Fluid Dynamics* (2012).
19. J. Hanotu, H. Bandulasena, and W. B. Zimmerman, "Microflotation performance for algal separation," Biotechnol. Bioeng. **109**, 1663–1673 (2012).
20. G. L. Chahine, (22nd October 2015). The ABS Acoustic Bubble Spectrometer (Dynaflow inc.). Available: http://www.dynaflow-inc.com/Products/ABS/ABS_General-Presentation.pdf
21. W. Sowa, "Interpreting mean drop diameters using distribution moments," Atomization Sprays **2**, 1–15, 1992.
22. G. Dunderdale, S. Ebbens, P. Fairclough, and J. Howse, "Importance of particle tracking and calculating the mean-squared displacement in distinguishing nanopropulsion from other processes," Langmuir **28**, 10997–11006 (2012).
23. M. Shirota, T. Sanada, A. Sato, and M. Watanabe, "Formation of a submillimeter bubble from an orifice using pulsed acoustic pressure waves in gas phase," Phys. Fluids (1994-present) **20**, p. 043301 (2008).
24. J. Lighthill, "Acoustic streaming," J. Sound Vibration **61**, 391–418 (1978).
25. T. Leighton, *The Acoustic Bubble* (Academic, 1994).
26. S. Brittle, P. Desai, W. C. Ng, A. Dunbar, R. Howell, V. Tesař, and W. B. Zimmerman, "Minimising microbubble size through oscillation frequency control," Chem. Eng. Res. Design **104**, 357–366 (2015).
27. W. B. Zimmerman, V. Tesar, S. Butler, and H. C. Bandulasena, "Microbubble generation," Recent Pat. Eng. **2**, 1–8 (2008).
28. J. Hanotu, H. C. H. Bandulasena, T. Y. Chiu, and W. B. Zimmerman, "Oil emulsion separation with fluidic oscillator generated microbubbles," Int. J. Multiphase Flow **56**, 119–125 (2013).
29. M. K. H. Al-Mashhadani, H. C. H. Bandulasena, and W. B. Zimmerman, "CO_2 mass transfer induced through an airlift loop by a microbubble cloud generated by fluidic oscillation," Ind. Eng. Chem. Res. **51**, 1864–1877 (2012).
30. J. Hanotu, E. Karunakaran, H. Bandulasena, C. Biggs, and W. B. Zimmerman, "Harvesting and dewatering yeast by microflotation," Biochem. Eng. J. **82**, 174–182 (2014).
31. Bubble analyzer JOSA.vi. file, figshare (2016). https://dx.doi.org/10.6084/m9.figshare.3462590.v1.
32. File to prompt user for input with enter key enabled_v2.vi., figshare (2016). https://dx.doi.org/10.6084/m9.figshare.3462593.v2.
33. Multi bubble calibration sub_v11 state machine.vi. file, figshare (2016). https://dx.doi.org/10.6084/m9.figshare.3462596.v1.